Three-dimensional catheter navigation of airways using continuous-sweep limited angle fluoroscopy on a C-arm

Martin G. Wagner[a], **Sarvesh Periyasamy**[b], **Sebastian Schafer**[c], **Paul F. Laeseke**[b] and **Michael A. Speidel**[a,d,*]

[a]University of Wisconsin–Madison, School of Medicine and Public Health, Department of Medical Physics, Madison, United States
[b]University of Wisconsin–Madison, School of Medicine and Public Health, Department of Radiology, Madison, United States
[c]Siemens Healthineers, Forchheim, Germany
[d]University of Wisconsin–Madison, School of Medicine and Public Health, Department of Medicine, Madison, United States

Abstract

Purpose: To develop an imaging-based 3D catheter navigation system for transbronchial procedures including biopsy and tumor ablation using a single-plane C-arm x-ray system. The proposed system provides time-resolved catheter shape and position as well as motion compensated 3D airway roadmaps.

Approach: A continuous-sweep limited angle (CLA) imaging mode where the C-arm continuously rotates back and forth within a limited angular range while acquiring x-ray images was used for device tracking. The catheter reconstruction was performed using a sliding window of the most recent x-ray images, which captures information on device shape and position versus time. The catheter was reconstructed using a model-based approach and was displayed together with the 3D airway roadmap extracted from a pre-navigational cone-beam CT (CBCT). The roadmap was updated in regular intervals using deformable registration to tomosynthesis reconstructions based on the CLA images. The approach was evaluated in a porcine study (three animals) and compared to a gold standard CBCT reconstruction of the device.

Results: The average 3D root mean squared distance between CLA and CBCT reconstruction of the catheter centerline was 1 ± 0.5 mm for a stationary catheter and 2.9 ± 1.1 mm for a catheter moving at ~ 1 cm/s. The average tip localization error was 1.3 ± 0.7 mm and 2.7 ± 1.8 mm, respectively.

Conclusions: The results indicate catheter navigation based on the proposed single plane C-arm imaging technique is feasible with reconstruction errors similar to the diameter of a typical ablation catheter.

 [DOI: 10.1117/1.JMI.8.5.055001]

Keywords: pulmonary interventions; 4D reconstruction; fluoroscopy; catheter tracking; C-arm.

Paper 21082R received Apr. 12, 2021; accepted for publication Oct. 1, 2021; published online Oct. 15, 2021.

1 Introduction

Transbronchial biopsy and tumor ablation are interventional procedures for the diagnosis and treatment of malignant pulmonary nodules,[1] wherein a catheter is navigated through the airways to the treatment site to extract a tissue sample or apply local therapy. Accurate localization of the catheter within the airways, both during navigation and at the final target location, is crucial for

*Address all correspondence to Michael A. Speidel, speidel@wisc.edu

2329-4302/2021/$28.00

the success of the procedure whilst minimizing complications. Current clinical practice mostly relies on bronchoscopy[2–5] for visualization during the procedure. However, the limited range of insertion, which makes it difficult to target smaller and more peripheral nodules, difficulties in navigating the bronchoscope, and a lack of 3D location information have prompted the use of additional imaging or alternative guidance techniques.[6–8]

X-ray fluoroscopic imaging is frequently used to assist with the guidance of bronchoscopes for the biopsy of pulmonary lesions.[5,9,10] It provides real-time 2D feedback of the device position and may be combined with static overlays of the airways from previously acquired MRI, CT, or CBCT images (augmented fluoroscopy).[11–13] However, navigating complex 3D structures can be challenging using 2D image guidance only and deformations of the airways due to respiration or the stiffness of the catheter are not represented accurately. Device-based imaging techniques such as fiberoptic bronchoscopy and endobronchial ultrasound (EBUS) can provide local imaging of the airways at the device tip without ionizing radiation, but do not provide information of the current device shape and position within the airways.[14,15] Alternative strategies, such as electromagnetic (EM) tracking and robotic bronchoscopy, have been proposed, all of which rely on previously acquired diagnostic CT or MRI images.[9,16–18] While these techniques promise to provide accurate 3D localization of the device in real-time, they require specialized equipment. In many cases, the required manual registration steps for each patient are time-consuming and the accuracy can degrade over the course of the procedure.[19] Additionally, while previously acquired diagnostic scans are generally available for most patients, registration to them is prone to error due to differences in patient position and respiration (CT-to-body divergence) and does not provide information on motion or deformation of the airways during the procedure.[20,21] Recently, techniques such as 4D fluoroscopy have been proposed, which allow 3D device reconstruction (e.g. catheters, guidewires, and prosthetic valves) from two simultaneously acquired x-ray images from different views.[22,23] However, these techniques require the use of biplane x-ray fluoroscopy systems, which are not as readily available as single plane systems in some clinical settings. Additionally, biplane acquisitions have the disadvantage of higher radiation dose compared to single plane acquisitions if the same frame rate is used.

Our work presents a single C-arm–based technique to address some of the limitations of previously proposed methods such as bi-plane-based 4D fluoroscopy. It provides high frame-rate 3D imaging of interventional devices such as catheters or bronchoscopes using fluoroscopic imaging and can be used by itself or in conjunction with bronchoscopy or EBUS to provide information on the shape and position of the device relative to the airways as well as local device-based imaging. In contrast to 4D fluoroscopy, which relies on simultaneous fluoroscopy imaging from different angles using a biplane system, our method only requires the more readily available single plane (single C-arm) x-ray fluoroscopy platform. The method consists of a specialized continuous-sweep limited angle (CLA) image acquisition mode and an iterative 3D device reconstruction technique for accurate high frame-rate catheter localization.

2 Methods

Figure 1 shows an overview of the proposed airway navigation system based on live CLA x-ray fluoroscopy. X-ray fluoroscopy over continuously changing angles allows for time-resolved 3D catheter reconstruction, which can be displayed within a pre-acquired anatomic roadmap using virtual endoscopic or semi-transparent rendering techniques.[22,24] The CLA fluoroscopy mode simultaneously provides image data for tomosynthesis reconstruction of the airways at regular intervals, which can be used to update the airway roadmap and compensate for motion or deformation. In the proposed clinical workflow, a pre-navigational, non-contrast cone beam CT (CBCT) is acquired to obtain an initial 3D airway roadmap, and the CBCT roadmap is updated throughout catheter navigation by performing a deformable registration between the CBCT volume and the tomosynthesis volumes reconstructed at regular intervals. Reconstruction and motion compensation algorithms were implemented on a research workstation (Precision 5810XL, Dell, Round Rock, Texas) with a 6-core processor (Xeon E5-1650, 3.6 Ghz, Intel, Santa Clara, California), 64 GB DDR4 memory, and a dedicated GPU (Geforce GTX 1080TI, NVIDIA, Santa Clara, California) using MATLAB R2020a.

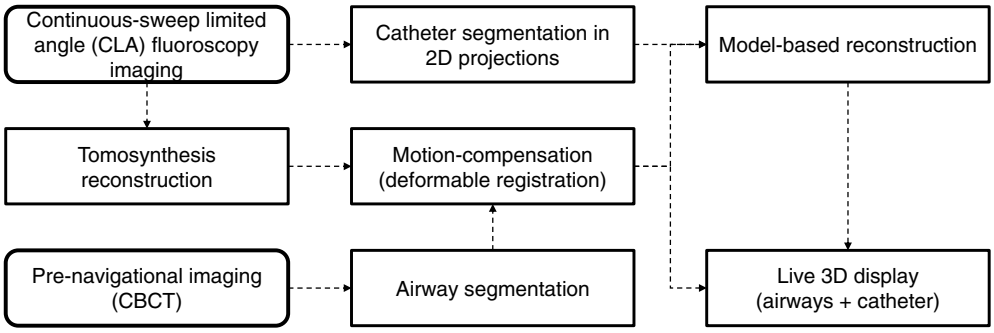

Fig. 1 Overview of the proposed single plane airway navigation system using continuous-sweep limited-angle fluoroscopy for 3D device reconstruction and tomosynthesis based motion compensation.

2.1 *Continuous-Sweep Limited Angle Fluoroscopy*

The foundation of the proposed single-plane imaging method is the CLA acquisition mode, which provides frame-by-frame 3D information on device position. Image acquisitions in this study were performed using an interventional C-arm system (Artis Zee, Siemens Healthineers, Forchheim, Germany) equipped with a 30×40 cm flat panel detector (1920×2480 pixels) with a native detector pitch of 0.154 mm. The imaging mode is a modification of an existing clinical 3D scanning protocol for cerebral perfusion imaging consisting of multiple back-and-forth rotational acquisitions.[25] In CLA fluoroscopy, the back-and-forth nature is retained to ensure that there are always recent images of the moving catheter from a range of projection angles, as is needed for 3D reconstruction, however the range of each sweep is limited to avoid interruptions to clinical workflow caused by full-sweep rotational acquisitions. Fig. 2 shows the C-arm motion during image acquisition using the CLA mode. A series of C-arm sweeps is performed over an angular range θ. Within this work, a range between -45 deg and 45 deg ($\theta = 90$ deg) relative to an anteroposterior projection angle was used, providing a maximum of 90 deg separation between images without impacting physician access to the patient. During each sweep, 59 projection images are acquired with an angular step size of $\beta = 1.5$ deg and a frame rate of 30 frames per second (fps). The time for a single sweep is 2.55 s followed by a break of $\sim$0.6 s required by the C-arm to change directions. In the present study, five sweeps were performed per scan resulting in a total acquisition time of $\sim$15 s. However, the total acquisition time can be as long or short as desired and up to 75 s on the current prototype. In practice, we envision the acquisition time to be extended dynamically while the user is pressing a foot pedal similar to conventional fluoroscopy. The projection matrices for each angle (in each direction) were determined in a one-time calibration step using a phantom with metal beads of two different sizes

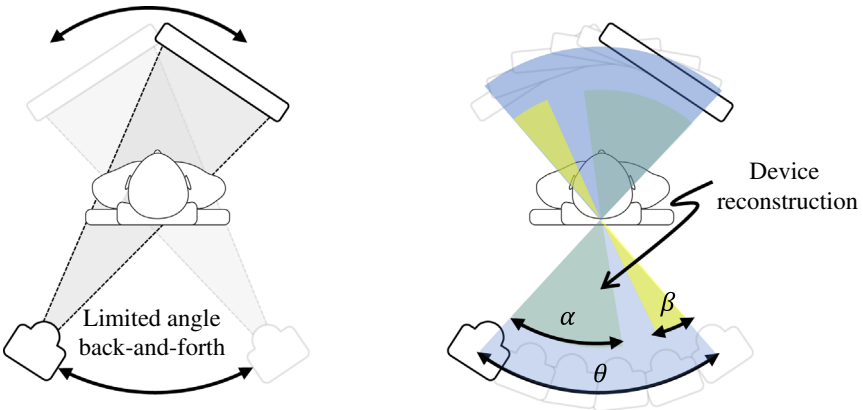

Fig. 2 C-arm motion for CLA fluoroscopy mode with total sweep angle θ, minimum angular increment β, and device reconstruction window α.

arranged in a helical shape. This geometric calibration is commonly performed for rotational C-arm acquisitions such as 3D CBCT protocols. Thus, existing software for the calibration of clinical C-arm systems[26] provided by the x-ray system manufacturer was used.

2.2 *3D Catheter Reconstruction*

The device reconstruction method is an extension of a recently proposed approach using a different model to represent the device.[27] The purpose of the modified approach was to increase accuracy and decrease computation time for the reconstruction. The proposed single plane device reconstruction algorithm uses a subset of the projection images acquired using the CLA fluoroscopy mode to determine the time-resolved shape and position of the catheter. The subset of projection images used for reconstruction is a sliding window of the past $n = 59$ image frames, corresponding to an angular reconstruction window of $\alpha \in [45\ \text{deg}; 90\ \text{deg}]$, equivalent to the maximum separation angle between any two frames in the subset. The maximum of 90 deg separation is reached when the projection angle of the last frame is either at -45 deg or 45 deg, whereas the minimum separation angle experienced when the projection angle of the last frame is 0 deg. In the latter case the projection angles in the sliding window range is $[0\ \text{deg},\ 45\ \text{deg}] \cup [45\ \text{deg},\ 0\ \text{deg}]$ or $[0\ \text{deg}, -45\ \text{deg}] \cup [-45\ \text{deg},\ 0\ \text{deg}]$ depending on the current rotation direction of the C-arm. Since the catheter position and shape might change within the sliding window, the reconstruction technique is designed to determine the shape and position of the catheter at the acquisition time of the most recent image frame, whereas the remaining frames are used to improve depth localization. The more recent frames generally provide a device representation that is closer to the current catheter position compared to the last frame but also havs smaller separating angles, which increase the depth localization error.[28] The opposite is the case for early frames with large angular separation, which provide more accurate depth localization but do not necessarily represent the latest device shape and position. Using a sliding window allows for catheter reconstruction at high frame rates, up to the frame rate of the image acquisition (30 fps).

For a given subset of projection images, the device reconstruction is performed by (1) segmenting the 2D centerline of the catheter from each projection image, and (2) iteratively optimizing a 3D model representing the catheter to minimize a cost function based on the similarity to the 2D device segmentations.

The catheter segmentation was performed using a convolutional neural network based on the SegNet architecture[29] and trained for the segmentation of guidewires in liver procedures.[30] For clutter removal, a connected component analysis was applied, where for the first image frame of the CLA acquisition, the largest connected component was selected, whereas for all other frames, all components overlapping with the segmentation of the preceding image frame were included. The centerlines were extracted using a topology preserving thinning approach[31] followed by a 2D path search.[22] Finally, each point along the centerline was refined to subpixel precision by fitting a Gaussian function to the cross profile of intensity (taken perpendicular to the centerline) and updating the centerline point to be the location of the maximum of the Gaussian fit.

A set of $m = 8$ control points was used as model for the reconstruction to describe the position and shape of the 3D catheter centerline. The number of control points is dictated by the flexibility of the device and was chosen empirically for the catheter used in this study. More flexible devices such as thin guidewires, might require a larger number of control points. The control points were connected by interpolating natural cubic splines using the centripedal model[32] for parameterization providing a smooth 3D curve passing through the control points. If each control point were positioned freely in 3D space, the model would have $3 \cdot m = 24$ deg of freedom. The number of degrees of freedom was reduced by leveraging the prior knowledge that each control point, when projected into the 2D space of the last projection image, has to lie on the segmented 2D centerline. In other words, the 3D location of all control points is limited to lie on the surface created by back-projecting the 2D device segmentation from the latest projection image into 3D space as shown in Fig. 3. Thus, the location of a control point can be represented by two parameters r_i and s_i (instead of three Cartesian coordinates), which describe (a) the corresponding position along the 2D centerline of the last projection image and (b) the depth of the control point s_i represented as the distance in mm from the focal point. The position

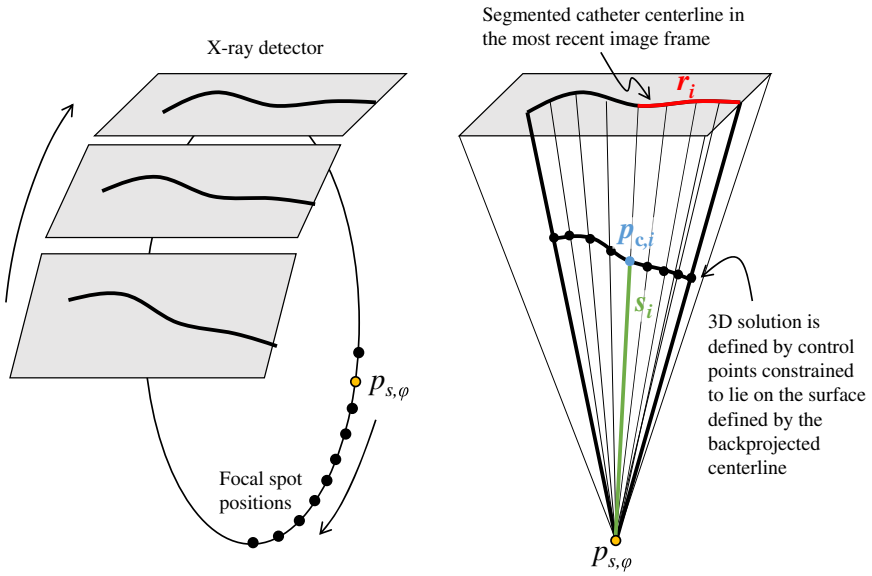

Fig. 3 Visualization of the device reconstruction approach. Left: x-ray images acquired from different focal spot positions $p_{s,\varphi}$ acquired during back-and-forth sweep of the imaging gantry while the device is navigated. Right: Representation of the device model control points $p_{c,i}$ using the position along the 2D centerline r_i and depth s_i.

along the 2D centerline is described by a scalar value r_i within the interval [0; 1] with 0 and 1 being the proximal and distal ends, respectively. It is worth noting that $r_0 = 0$ is implicitly defined and is not part of the optimization procedure. The total number of degrees of freedom is therefore $2m - 1$. In the following sections, the vectors containing all variables r_i and s_i are referred to as $\boldsymbol{r}$ and $\boldsymbol{s}$, respectively. The relationship between the two parameters $[r_i,\ s_i]$ of the i'th 3D control point and the corresponding representation as 3D Cartesian coordinates $\boldsymbol{p}_{\mathrm{c},i}$ is

$$\boldsymbol{p}_{\mathrm{c},i} = \boldsymbol{p}_{\mathrm{s},\varphi} + s_i \cdot \frac{\boldsymbol{q}_i}{\boldsymbol{q}_i}, \tag{1}$$

where $\boldsymbol{p}_{\mathrm{s},\varphi}$ is a three-element vector representing the 3D focal spot location for a given projection angle φ and $\boldsymbol{q}_i$ is a direction vector pointing from a given 2D image point to the focal spot calculated by multiplying the inverse Q_φ of the upper left 3×3 elements of the projection matrix with the 2D pixel coordinates corresponding to the control point location along the segmented centerline

$$\boldsymbol{q}_i = Q_\varphi \cdot \begin{bmatrix} u_\varphi(r_i) \\ v_\varphi(r_i) \\ 1 \end{bmatrix}. \tag{2}$$

The functions $u_\varphi(r_i)$ and $v_\varphi(r_i)$ represent the 2D coordinates of a point along the segmented catheter centerline of projection angle α, linearly interpolated at position r_i, where r_i is the relative position along the centerline represented by a value in the interval [0; 1].

The cost function used for the iterative reconstruction is comprised of a data fidelity term describing the similarity between the 3D model and the 2D images, and three regularization terms. The data fidelity term is calculated by interpolating a set of 100 points $\boldsymbol{p}_{\mathrm{3D,j}}(\boldsymbol{r},)$ distributed along the 3D spline curve and performing a forward projection into each of the image frames in the narrow angular range under consideration using the pre-calibrated projection matrices. The data fidelity d_{k} is calculated in terms of the mean squared distance (MSD) between the forward projected points and the corresponding points in the 2D centerline segmentation, where k denotes the frame index in the reconstruction window. This can be written as

$$d_k(\boldsymbol{r},\boldsymbol{s}) = \sum_{j=0}^{j<100} \left(\boldsymbol{h}_{2D} \left(P_\varphi \cdot \begin{bmatrix} \boldsymbol{p}_{3D,j}(\boldsymbol{r},\boldsymbol{s}) \\ 1 \end{bmatrix} \right) - \begin{bmatrix} u_\varphi(\dot{r}_j) \\ v_\varphi(\dot{r}_j) \end{bmatrix} \right)^2, \tag{3}$$

where P_φ is the projection matrix corresponding to gantry angle φ, $\boldsymbol{h}_{2D}$ is a function that divides all components of a 2D homogeneous vector by its third component and $\dot{r}_j$ is the position along the segmented 2D centerline corresponding to point $\boldsymbol{p}_{3D,j}(\boldsymbol{r},\boldsymbol{s})$. The parameter $\dot{r}_j$ is chosen such that the 2D path length from the most proximal point of the device is the same for both segmentation and forward projection of the spline model.

The data fidelity term for the k-th image frame acquired at time $t(k)$ is weighted using a scaling factor $\lambda_{t(k)}$ based on the time difference from the most recent image acquired at t_0, where

$$\lambda_{t(k)} = \exp\left(-\frac{(t(k)-t_0)^2}{\sigma^2} \right). \tag{4}$$

The weighting factor places higher emphasis on more recently acquired projection images, where the device position and shape are likely to be similar to the latest frame. The parameter σ regulates the balance between temporal resolution and depth resolution and was chosen empirically to be $\sigma = 1.7 \cdot n$, where n is the number of projection images in the sliding window.

Three regularization terms were added to the cost function to include prior knowledge and improve reconstruction accuracy. Regularization parameters included the 3D curvature $\kappa_i(r_i, s_i)$ at each of the control points to account for the stiffness of the catheter, the average Euclidean distance $d_{\text{prev}}(\boldsymbol{r},\boldsymbol{s})$ of all points $\boldsymbol{p}_{3D,j}(\boldsymbol{r},\boldsymbol{s})$ of the current solution to the previous reconstruction to smooth catheter motion over time, and the average distance of the 3D catheter points to the airway roadmap $d_{\text{rm}}(\boldsymbol{r},\boldsymbol{s})$, which is zero for points inside of the airway lumen. The overall cost function can be written as

$$f_{\text{cost}}(\boldsymbol{r},\boldsymbol{s}) = \sum_{k=0}^{n} \lambda_{t(k)} d_k(\boldsymbol{r},\boldsymbol{s}) + \gamma_1 d_{\text{prev}}(\boldsymbol{r},\boldsymbol{s}) + \gamma_2 d_{\text{rm}}(\boldsymbol{r},\boldsymbol{s}) + \gamma_3 \sum_{i=0}^{m} \kappa_i(r_i, s_i), \tag{5}$$

where γ_1, γ_2, and γ_3 are weighting factors controlling the cost for large changes of the device shape and position between consecutive frames, device centerline points outside the airway roadmap, and the device curvature, respectively. The cost minimization is performed using the Nelder-Mead simplex approach with a termination tolerance of $1e^{-5}$ on the function value and the parameter estimate. For 8 control points, the optimization procedure has $8 \cdot 2 - 1 = 15$ degrees of freedom.

The goal of the optimization procedure is to find the parameter vectors $\boldsymbol{r}$ and $\boldsymbol{s}$ defining the 3D control points, which minimize the cost function. Every valid solution must have the properties $r_0 = 0$, $r_m = 1$ and $r_{i-1} < r_i$ for $0 < i \leq m$ to ensure that the first and last control points always correspond to the proximal and distal ends of the centerline and to ensure monotonicity of the centerline. Instead of using a constrained optimization process to enforce these conditions, the parameter vector $\boldsymbol{r}$ is re-expressed using a set of parameters $\tilde{r}_i$ describing the relative distance of the i-th control point to the previous control point such that

$$r_i = \frac{\sum_{j=1}^{i} |\tilde{r}_j|}{\sum_{k=1}^{m} |\tilde{r}_k|}. \tag{6}$$

This guarantees both monotonicity and endpoint constraints and allows the use of any unconstrained optimizer.

The cost minimization is initialized using the control point positions reconstructed for the previous sliding window position (time frame). For the first time frame, where no previous reconstruction is available, an initial reconstruction is performed using the two-view reconstruction technique described in Wagner et al,[22] where the first and last frame of the subset were used as input images. The initial first-frame centerline is then converted to control points by minimizing the root mean squared distance (RMSD) between a spline curve represented by the

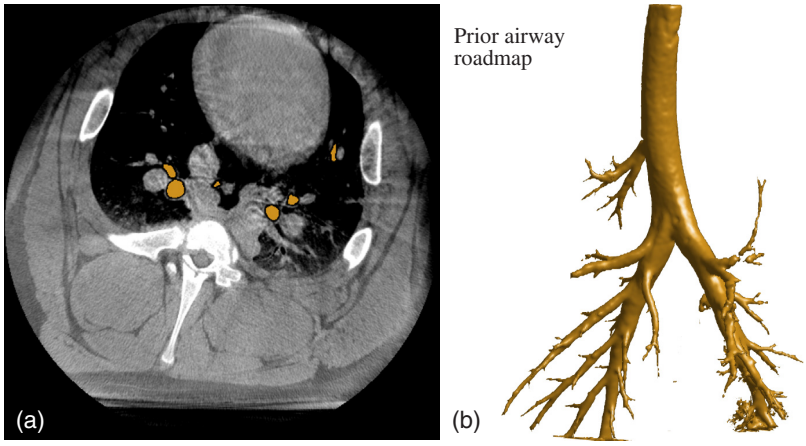

Fig. 4 (a) Central CBCT slice with airway segmentation (beige). (b) Surface rendering of the segmented airway roadmap from prior CBCT.

control points and the centerline. The control points are then used as initialization to minimize f_{cost} for the first frame.

2.3 *Motion-Compensated Airway Roadmap*

An initial airway roadmap was generated from the pre-navigational CBCT acquisition ($512 \times 512 \times 392$ voxel, 0.47-mm homogenous voxel size). A Gaussian filter ($\sigma = 1$ pixels) was applied to the 3D CBCT followed by global thresholding ($\tau = -615$ HU) to segment the low attenuation values within the airways from the surrounding lung tissue. Since the air outside the body is also segmented, a connected component analysis was applied to each slice of the 3D volume, where the largest component (representing the surrounding air) was removed. Figure 4 shows an example of a central CBCT slice through the lung along with the airway segmentation.

To account for airway motion or deformation during catheter navigation, the roadmap was updated in regular intervals based on the CLA projection image data. For this purpose, limited angle tomosynthesis reconstruction was performed after each 90-deg C-arm sweep. Projection data was pre-processed (I_0 normalization, ramp filtering) and reconstructed using the pre-calibrated projection matrices for the system.[33] A deformable registration approach (DEMONS) was used to estimate a deformation vector field (DVF) between the initial CBCT volume and the tomosynthesis reconstruction.[34,35] Prior to registration, the high-intensity catheter was removed from the tomosynthesis volume through thresholding, eliminating high-intensity inconsistencies between the two volumes. The segmented roadmap derived from the baseline CBCT was than deformed based on the DVF.

2.4 *Evaluation*

A porcine study was performed to evaluate the feasibility and accuracy of the proposed techniques. Approval for this study was received from the local Institutional Animal Care and Use Committee (IACUC). A total of eight catheter navigation sequences were acquired in three female pigs (weight 50 to 55 kg) using the CLA imaging mode. A pre-navigational CBCT was acquired for each pig to establish the 3D airway roadmap. To simplify the image acquisition, CLA acquisitions were performed during the pullback of a catheter and guidewire and the recorded image frame reversed retrospectively to simulate forward motion. Therefore, conventional 2D fluoroscopy was used to place a transbronchial catheter (and guidewire) in a distal airway branch. After catheter placement, a non-contrast CBCT was acquired to establish a gold standard of the catheter shape and position by performing a global thresholding step followed by centerline extraction.[31] The CLA imaging mode was then used to acquire x-ray projection images, whereas the catheter and guidewire were pulled back. Both CBCT and CLA acquisitions were performed during breath holds to reduce respiratory motion. After reversing the order of the

projection images, the catheter was reconstructed retrospectively for each sliding window position in the sequence and the final reconstruction was compared to the gold standard CBCT. Reconstruction accuracy was determined using the RMSD and the tip localization error (TLE) representing the Euclidean distance between the most distal catheter points of the reconstruction and gold standard, respectively. Finally, the percentage of time frames was calculated where the reconstructed catheter tip was within the airway roadmap, as an overall indicator of reconstruction fidelity.

3 Results

The device reconstruction was performed with a frame rate of 30 fps using a sliding window of 59 frames representing a time difference between the first and last frame of 2.55 s. The weighting factors were chosen empirically ($\gamma_1 = 50$, $\gamma_2 = 1000$, and $\gamma_3 = 100$). The average device tip velocity was between 0.8 and 1.1 cm/s (estimated based on the difference of the device length between the pre- and post-pullback CBCT acquisitions), corresponding to an average displacement of 2 to 3 mm within each sliding window. The lengths of the reconstructed device centerlines at the most distal position (last frame) ranged between 5.6 and 19.7 cm.

The average 3D RMSD between the catheter reconstruction from the last frame of each CLA sequence compared to the gold standard was 1 ± 0.5 mm for a stationary catheter and 2.9 ± 1.1 mm for a catheter moving at ~1 cm/s. For reference, the typical ablation catheter diameter is ~2 mm.[36] The average TLE, calculated as the Euclidean distance between the most distal point of the CLA reconstruction and the reference centerline extracted from the pre-pullback CBCT, ranged from 1.3 ± 0.7 mm (static device) to 2.7 ± 1.8 mm (moving device). In $88.6 \pm 10.8\%$ of the frames, the location of the distal catheter tip was located within the lumen of the airway roadmap. When the reconstructed tip was outside of the roadmap, the average distance of the tip location to the roadmap was 0.63 ± 0.56 mm. The individual results for all cases are listed in Table 1.

Examples of 3D visualizations of the CLA device reconstructions within the airway roadmap are shown in Fig. 5 for different cases and different time frames. The figure also shows a

Table 1 Individual results for all pig studies and catheter navigation sequences: Columns 1 and 2 show the TLE and RMSD along the body of the device compared to the gold standard CBCT for a static device (no motion during CLA sweep). Columns 3 and 4 show the same results for the last frame (most distal device position) of a moving device (~1 cm/s). Column 5 is the percentage of image frames where the reconstructed device tip is inside of the airway roadmap. The last column shows the average Euclidean distance of tip locations to the airway roadmap when the reconstructed tip is located outside of the airway roadmap.

Case	TLE	RMSD	TLE	RMSD	Inside (%)	Distance
	(Static device)		(Moving device)			
Seq #1 (Pig A)	1.6 mm	1.3 mm	2.5 mm	3.5 mm	96.6	0.2 mm
Seq #2 (Pig B)	2.1 mm	0.7 mm	1.7 mm	3.0 mm	94.5	0.5 mm
Seq #3 (Pig B)	1.2 mm	0.9 mm	6.8 mm	4.5 mm	76.8	1.7 mm
Seq #4 (Pig B)	0.3 mm	2.1 mm	3.4 mm	1.6 mm	97.9	0.2 mm
Seq #5 (Pig C)	0.8 mm	0.8 mm	1.6 mm	3.5 mm	99.2	0.1 mm
Seq #6 (Pig C)	1.9 mm	0.6 mm	1.7 mm	1.8 mm	87.3	0.4 mm
Seq #7 (Pig C)	0.5 mm	0.8 mm	2.8 mm	1.5 mm	87.3	0.9 mm
Seq #8 (Pig C)	1.7 mm	1.0 mm	1.2 mm	3.6 mm	69.2	1.2 mm
Average ± STD	**1.3 ± 0.7 mm**	**1.0 ± 0.5 mm**	**2.7 ± 1.8 mm**	**2.9 ± 1.1 mm**	**88.6 ± 10.8**	**0.7 ± 0.5 mm**

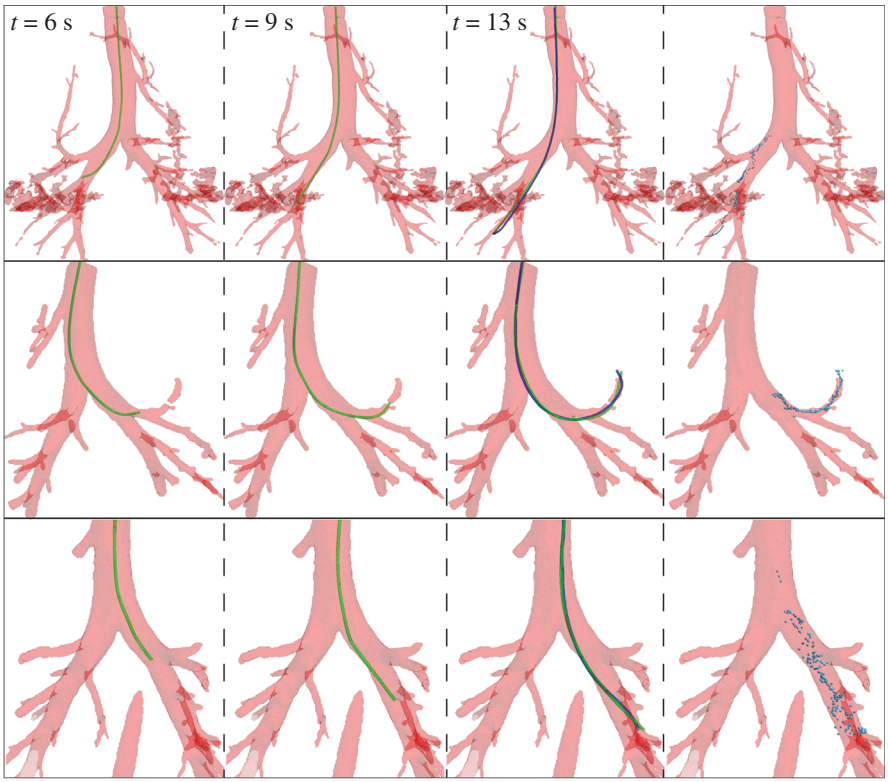

Fig. 5 3D renderings of the CLA device reconstructions (green) for three different cases (rows). The first three columns represent different time frames at 6, 9, and 13 s after the start of the sequence, respectively. The third column is the last frame of the sequence, which also includes the gold standard device position (blue). The last column shows all device tip positions during the acquisition sequence.

comparison between the CLA reconstruction of the last time frame and the gold standard extracted from CBCT. The last column shows all device tip locations during the sequence as individual spheres. Fig. 6 shows intermediate steps of the single-plane reconstruction approach with the segmented 2D catheter [Fig. 6(a)] and the first and last frame of the reconstruction window with the estimated spline model and control points superimposed [Figs. 6(b) and 6(c)]. In this example the catheter is moving, and the model shown is representative of the time point corresponding to the last frame. Therefore, as expected, when the model is forward

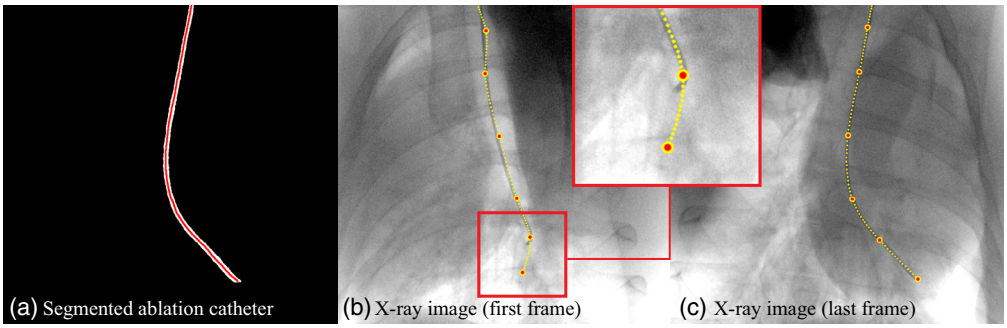

Fig. 6 Single-plane device reconstruction method. (a) Binarized fluoroscopy image (last frame) with device centerline. Panels (b) and (c) are the first and last fluoroscopy frames of a sliding reconstruction window with reconstructed device control points corresponding to the last frame and path superimposed as yellow line and red dots. The device reconstruction was derived from all frames in the reconstruction window including the x-ray images shown in (b) and (c).

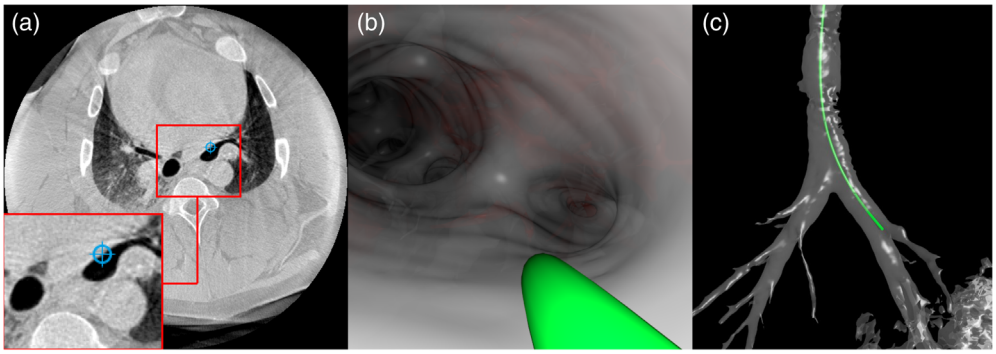

Fig. 7 Three different visualization techniques for device navigation based on CLA reconstruction showing the same time frame: (a) axial view through the CBCT volume with the device tip shown with blue cross hairs (inset shows a magnification of the region with the device), (b) virtual endoscopic view with device shown as a green tubular structure (virtual camera placed just behind the device tip), (c) 3D rendering with a semi-transparent airway surface and the device shown as a green tubular structure.

projected and superimposed on the first image frame as in Fig. 6(b), the tip position in the x-ray image does not line up with the tip position of the model.

The proposed CLA-based device reconstruction in combination with the pre-navigational CBCT allows for different visualization techniques, which could be used to aid in the navigation such as cut-plane views through the CBCT volume with virtual device tip, virtual endoscopic views and 3D renderings with semi-transparent airway surfaces. Figure 7 shows examples of these three visualization techniques for the same time frame in a navigational sequence generated retrospectively using MATLAB R2020a (axial view) and the open-source software Blender 2.79b (endoscopic and semi-transparent view). In practice, these visualizations could be shown side-by-side or specific views could be selected based on user preferences and would be updated dynamically as the probe moves.

4 Discussion

This work presents a high frame-rate (30 fps) 3D image guidance technique for transbronchial biopsies and ablations using widely available single plane (single C-arm) x-ray systems, which could provide real-time information on catheter device location within the airways without the need for specialized equipment. The enabling technology is the CLA imaging mode, which leverages the ability of the C-arm to perform small back-and-forth angular sweeps to obtain continuously updated 3D information on the catheter and airway anatomy. An iterative, model-based approach was developed to reconstruct the catheter shape from a sliding window of image frames corresponding to a range of projection angles, and a temporal weighting scheme was introduced to allow for the possibility that each projection image might represent a slightly different device position due to device motion. Finally, it is demonstrated how the images acquired in CLA mode can also be used to perform shift-and-add tomosynthesis during device navigation. These tomosynthesis images may be used to update a pre-navigational CBCT airway roadmap using CBCT-to-tomosynthesis registration, enabling time-resolved 3D display of both catheter device and airway roadmap.

For a stationary catheter, accuracies of 1 mm (RMSD) and 1.3 mm (TLE) were achieved. These values increased to 2.7 and 2.9 mm for RMSD and TLE respectively when the catheter was moving. The higher localization error for a moving device can be expected. Since the catheter is moving at 1 cm/s and the time difference between first and last frame of each sliding window is 2.55 s, the difference in visible device length would be up to 2.55 cm. Since the distal end of the device is only present in a very narrow angular range of the sliding window, depth localization of these points largely depends on regularization using the assumption of a stiff catheter. Nevertheless, the reconstruction error for moving catheters was found to be comparable to the typical ablation catheter diameter of approximately 2 mm and smaller than

lesions currently targeted during transbronchial biopsies or ablations (>5 mm).[36] Previously reported accuracy results for alternative strategies such as EM-tracking and EBUS with simultaneous localization and mapping (SLAM) approach are usually on the order of 4 mm and higher.[37–39] Additionally, Leong et al.[40] defined a registration error <5 mm as acceptable for device navigation during bronchoscopic procedures. For this feasibility study, computation time was not a primary focus and the prototype was implemented in MATLAB without optimization, multi-threading or GPU processing. In this study, average computation times for the device reconstruction were 8.1 $\pm$ 1.5 s, however, with optimization and GPU processing[41,42] clinically relevant frame rates of 15 frames per second or higher should be achievable.

The main limitations of this study were the relatively small number of subjects (three animals) and the use of catheter pullbacks rather than forward motion. A prospective study with a larger number of subjects and real-time guidance is needed to validate the findings of this study and to evaluate the benefits of this technique with respect to accurate navigation to specific targets. Such a study should also include an investigation into the different parameters of the imaging mode such as the sweep duration, angular step size, and angular range, which can be varied. Additionally, this study uses breath holds during device navigation to avoid respiratory motion. Due to the relatively long window used for tomosynthesis relative to the typical time of a respiratory cycle (2.55 s compared to 3 to 5 s) the proposed registration of the initial CBCT to tomosynthesis reconstruction is best suited for slowly changing deformations such as diaphragm drift and deformation of airways due to the catheter stiffness. Future work should investigate shorter windows as well as retrospective gating for tomosynthesis reconstruction to account for respiratory motion. Finally, while not a primary focus of this study, the proposed C-arm–based device navigation system requires radiation exposure. If CLA acquisitions are performed at similar dose levels and with similar frame rates as conventional fluoroscopy, the integral dose to the patient and operator dose from scatter is expected to be comparable to procedures guided using conventional or augmented fluoroscopy. However, a reduction of patient skin dose compared to fixed-view-angle fluoroscopy is expected due to the spreading of primary x-rays over a larger area at the patient entrance. Although radiation exposure presents a disadvantage of this technique over device-based imaging techniques such as bronchoscopy or EBUS, interventional x-ray imaging is routinely performed with similar dose levels in other current vascular and non-vascular percutaneous procedures and the added benefit of 3D device localization and image-based motion compensation of the airways could help improve placement accuracy and reduce procedure time.

Overall, the study showed promising results with device localization errors similar to or smaller than those reported for alternative strategies such as EM-tracking (4 to 6 mm).[37–39] Additionally, our technique provides a reconstruction of the full catheter shape including the body, compared to the tip only for most of the previously proposed techniques. The CLA imaging mode would cause minimal interruptions to the clinical workflow due to the very narrow angular range compared to conventional 3D acquisition protocols. Finally, the CLA-based approach could be implemented on clinical and widely available single-plane C-arm systems without the need for specialized devices or hardware.

5 Conclusion

A method for 3D catheter navigation during transbronchial biopsies or ablation procedures using a single C-arm x-ray system has been proposed. In an initial animal study, the technique yielded frame-by-frame reconstruction of the catheter shape and position for a moving catheter with an accuracy comparable to the device diameter. The proposed system could be deployed on widely available conventional x-ray systems without the need for adjunct device-specific navigation technologies. Future work should prospectively evaluate this technique using a real-time implementation.

Disclosures

The authors have no relevant financial interests in this manuscript.

Acknowledgments

Funding was received from Siemens Healthineers. Research reported in this publication was also supported by the National Heart, Lung, and Blood Institute under award number 5R01HL116567 and the National Institute of Biomedical Imaging and Bioengineering under award number R21EB024553. Additional funding was received from the National Cancer Institute under award number F30CA250408, and from the National Institute of General Medical Sciences under award number T32GM140935. The content is solely the responsibility of the authors and does not necessarily represent the official views of the National Institutes of Health. The concepts presented in this paper are based on research and are not commercially available.

References

1. H.-B. Yuan et al., "Flexible bronchoscopy-guided microwave ablation in peripheral porcine lung: a new minimally-invasive ablation," *Transl. Lung Cancer Res.* **8**(6), 787–796 (2019).
2. I. Valentini et al., "Competence in flexible bronchoscopy and basic biopsy technique," *Panminerva Med.* **61**(3), 232–248 (2019).
3. J. Wälscher and D. Gompelmann, "[Bronchoscopy]," *Dtsch. Med. Wochenschr.* **141**(17), 1236–1238 (2016).
4. S. Fernández-Bussy et al., "[Bronchoscopy with transbronchial biopsy for the diagnosis of potentially malignant pulmonary lesions: experience in 261 patients]," *Rev. Med. Chil.* **143**(4), 433–438 (2015).
5. V. Livi et al., "Competence in navigation and guided transbronchial biopsy for peripheral pulmonary lesions," *Panminerva Med.* **61**(3), 280–289 (2019).
6. P. Lee, "MTP13-01: indications and limitations of bronchoscopy," *J. Thoracic Oncol.* **2**(8), S278–S281 (2007).
7. F. Asano, "Advanced bronchoscopy for the diagnosis of peripheral pulmonary lesions," *Respir. Invest.* **54**(4), 224–229 (2016).
8. K. M. Horton, M. R. Horton, and E. K. Fishman, "Advanced visualization of airways with 64-MDCT: 3D mapping and virtual bronchoscopy," *Am. J. Roentgenol.* **189**(6), 1387–1396 (2007).
9. N. T. Tanner et al., "Standard bronchoscopy with fluoroscopy vs thin bronchoscopy and radial endobronchial ultrasound for biopsy of pulmonary lesions: a multicenter, prospective, randomized trial," *Chest* **154**(5), 1035–1043 (2018).
10. I. A. D. Rand et al., "British Thoracic Society guideline for diagnostic flexible bronchoscopy in adults: accredited by NICE," *Thorax* **68**(Suppl. 1), i1–i44 (2013).
11. T. Steger and M. Hoßbach, "Navigated bronchoscopy using intraoperative fluoroscopy and preoperative CT," in *9th IEEE Int. Symp. Biomed. Imaging*, pp. 1220–1223 (2012).
12. M. A. Pritchett et al., "Cone-beam CT with augmented fluoroscopy combined with electromagnetic navigation bronchoscopy for biopsy of pulmonary nodules," *J. Bronchol. Interven. Pulmonol.* **25**(4), 274–282 (2018).
13. D. K. Hogarth, "Use of augmented fluoroscopic imaging during diagnostic bronchoscopy," *Future Oncol.* **14**(22), 2247–2252 (2018).
14. X. Zang et al., "Optimal route planning for image-guided EBUS bronchoscopy," *Comput. Biol. Med.* **112**, 103361 (2019).
15. J. M. Liebler and C. J. Markin, "Fiberoptic bronchoscopy for diagnosis and treatment," *Critical Care Clinics* **16**(1), 83–100 (2000).
16. K. A. Khan et al., "Navigational bronchoscopy for early lung cancer: a road to therapy," *Adv Ther* **33**, 580–596 (2016).
17. A. C. Chen et al., "Accuracy of a robotic endoscopic system in cadaver models with simulated tumor targets: ACCESS study," *Respiration* **99**(1), 56–61 (2020).
18. W. D. Bolton et al., "Electromagnetic navigational bronchoscopy reduces the time required for localization and resection of lung nodules," *Innovations (Phila)* **12**(5), 333–337 (2017).
19. H. Olav Leira et al., "Navigated bronchoscopy with electromagnetic tracking-cone beam computed tomography influence on tracking and registration accuracy," *J Bronchology Interv Pulmonol* **18**(4), 329–336 (2011).

20. M. A. Pritchett et al., "Virtual or reality: divergence between preprocedural computed tomography scans and lung anatomy during guided bronchoscopy," *J Thorac Dis* **12**(4), 1595–1611 (2020).
21. K. Bhadra et al., "Lung navigation ventilation protocol to optimize biopsy of peripheral lung lesions," *J Bronchology Interv Pulmonol* (2021).
22. M. Wagner et al., "4D interventional device reconstruction from biplane fluoroscopy," *Med Phys* **43**(3), 1324–1334 (2016).
23. M. G. Wagner et al., "A dynamic model-based approach to motion and deformation tracking of prosthetic valves from biplane x-ray images," *Med Phys* **45**(6), 2583–2594 (2018).
24. M. G. Wagner et al., "Biplane reconstruction and visualization of virtual endoscopic and fluoroscopic views for interventional device navigation," *Proc. SPIE* **9786**, 978613 (2016).
25. A. Ganguly et al., "Cerebral CT perfusion using an interventional C-arm imaging system: cerebral blood flow measurements," *AJNR Am J Neuroradiol* **32**(8), 1525–1531 (2011).
26. K. Yang et al., "A geometric calibration method for cone beam CT systems," *Med Phys* **33**(6), 1695–1706 (2006).
27. M. G. Wagner et al., "Method for 3D navigation of airways on a single C-arm using multi-sweep limited angle acquisition and frame-by-frame device reconstruction," *Proc. SPIE* **11598**, 115980O (2021).
28. A. Brost et al., "Geometric accuracy of 3-D x-ray image-based localization from two C-arm views," in *Workshop Geom. Accuracy Image Guided Interventions-Medical Image Computing and Computer Assisted Interventions*, MICCAI, pp. 12–19, Citeseer (2009).
29. V. Badrinarayanan, A. Kendall, and R. Cipolla, "SegNet: a deep convolutional encoder-decoder architecture for image segmentation," *IEEE Trans. Pattern Anal. Mach. Intell.* **39**(12), 2481–2495 (2017).
30. M. G. Wagner, P. Laeseke, and M. A. Speidel, "Deep learning based guidewire segmentation in x-ray images," *Proc. SPIE* **10948**, 1094844 (2019).
31. M. G. Wagner, "Real-time thinning algorithms for 2D and 3D images using GPU processors," *J Real-Time Image Process.* **17**, 1255–1266 (2020).
32. E. T. Y. Lee, "Choosing nodes in parametric curve interpolation," *Comput.-Aided Des.* **21**(6), 363–370 (1989).
33. Y. Zhang et al., "A comparative study of limited-angle cone-beam reconstruction methods for breast tomosynthesis," *Med Phys* **33**(10), 3781–3795 (2006).
34. P. Muyan-özçelik et al., "Fast deformable registration on the GPU: a CUDA implementation of demons," in *Int. Conf. Comput. Sci. and Appl.* (2008).
35. M. M. McCormick et al., "ITK: enabling reproducible research and open science," *Front Neuroinform* **8**, 13 (2014).
36. J. R. Stevenson and B. S. Ashar, "Indications for use: NEUWAVE flex microwave ablation system and accessories," Department of Health and Human Services, Food and Drug Administration, 2017, https://www.accessdata.fda.gov/cdrh_docs/pdf16/K163118.pdf (accessed 9 April 2021).
37. S. N. Lavasani et al., "Compensation of dynamic electromagnetic field distortion using simultaneous localization and mapping method with application in endobronchial ultrasound-transbronchial needle aspiration (EBUS-TBNA) guidance," *Int. J. Med. Rob.* **16**(1), e2035 (2020).
38. D. Makris et al., "Electromagnetic navigation diagnostic bronchoscopy for small peripheral lung lesions," *Eur. Respir. J.* **29**(6), 1187–1192 (2007).
39. T. Sato et al., "Diagnostic yield of electromagnetic navigational bronchoscopy: results of initial 35 cases in a Japanese Institute," *J. Thorac. Dis.* **10**(S14), S1615–S1619 (2018).
40. S. Leong et al., "Electromagnetic navigation bronchoscopy: a descriptive analysis," *J Thorac. Dis.* **4**(2), 173–185 (2012).
41. B. J. Davis et al., "Evaluation of real-time guidewire navigation using virtual endoscopic 4D fluoroscopy," *Proc. SPIE* **11315**, 1131515 (2020).
42. M. G. Wagner et al., "Real-time 3D image fusion system for valvular interventions based on echocardiography and biplane x-ray fluoroscopy," *Proc. SPIE* **10951**, 1095121 (2019).

Martin G. Wagner received his doctorate from the University of Heidelberg, Germany, in 2014. He currently works as a senior scientist at the Department of Medical Physics, University of Wisconsin–Madison. His research interests include interventional (real-time) imaging, therapy targeting, multimodal fusion, and machine learning.

Sarvesh Periyasamy is an MD-PhD candidate at the University of Wisconsin School of Medicine and Public Health. His research interests include the development of novel imaging techniques for improving minimally-invasive image-guided interventions. He will be pursuing post-graduate residency training in Interventional Radiology.

Sebastian Schafer is working on the development and productization of next-generation interventional oncology imaging and guidance solutions for Siemens Healthineers. The focus of his career is the advancement of minimally invasive interventions through integration of therapy and imaging devices.

Paul F. Laeseke received his MD and PhD from the University of Wisconsin–Madison, in 2007 and 2009, respectively. He is currently an assistant professor in the Interventional Radiology section at the University of Wisconsin as well as co-director of the University of Wisconsin Image-Guided Interventions Lab. His research interests include quantitative interventional imaging techniques and interventional oncology, in particular ablative therapies.

Michael A. Speidel is an associate professor of Medical Physics and Medicine at the University of Wisconsin–Madison and co-director of the Image-guided Interventions Lab. The mission of this lab is to develop novel imaging tools for interventional radiologists and cardiologists through the application of physics, advanced imaging technology, and innovative algorithms.